

A diagram for the evaporation status of extrasolar planets

A. Lecavelier des Etangs

Institut d'Astrophysique de Paris, CNRS, UMR7095 ; Université Pierre et Marie Curie-Paris6, 98^{bis} boulevard Arago, F-75014 Paris, France

Received ...; accepted ...

ABSTRACT

Aims. To describe the evaporation status of the extrasolar planets, we propose to consider an energy diagram in which the potential energy of the planets is plotted versus the energy received by the upper atmosphere.

Methods. Here we present a basic method to estimate these quantities. For the potential energy, we include the modification of the gravity field by the tidal forces from the parent stars.

Results. This description allows a quick estimate of both the escape rate of the atmospheric gas and the lifetime of a planet against the evaporation process. In the energy diagram, we find an evaporation-forbidden region in which a gaseous planet would evaporate in less than 5 billion years. With their observed characteristics, all extrasolar planets are found outside this evaporation-forbidden region. The escape rates are estimated to be in the range 10^5 g s^{-1} to 10^{12} g s^{-1} , with few cases above 10^{11} g s^{-1} . The estimated escape rate for HD 209458 b is found to be consistent with the lower limit of 10^{10} g s^{-1} obtained from interpretation of the H I Lyman- α observations.

Finally, this diagram suggests possibilities for the nature of the recently discovered Neptune-mass planets. We find that GJ 436 b, 55 Cnc e and HD 69830 b cannot be low mass gaseous planets. With density necessarily above 0.5 g cm^{-3} to survive evaporation, these planets must contain a large fraction of solid/liquid material. Concerning GJ 876 d, we find that it must have a density larger than $\sim 3 \text{ g cm}^{-3}$ to survive the strong EUV energy flux from its nearby parent star. GJ 876 d must contain a large fraction of massive elements.

Key words. Stars: planetary systems

1. Introduction

Among the nearby two hundreds extrasolar planets identified today, there is a particular class of planets very close to their parent stars with semi major axis $\lesssim 0.1 \text{ AU}$. Among them, there are massive hot-Jupiters (also named “Pegasides”, Guillot et al. 1996) and small mass planets (see for instance, Santos et al. 2004; Rivera et al. 2005). These planets constitute about 20% and 5% respectively, of the planets identified today. Since the discovery of the first of them, 51 Peg b (Mayor & Queloz 1995), the issue of their evaporation status has been raised (Burrows & Lunine 1995; Guillot et al. 1996). Since these planets exist and orbit stars which are not particularly young, it is clear that the evaporation rate of the observed massive hot-Jupiters should be modest enough to not dramatically impact their evolution. At least they can survive billion years at the place where they are observed. It is extremely unlikely that we are witnessing a transient phase in the evolution of extrasolar planets (Baraffe et al. 2004). In brief, the discoveries of a large number of massive

hot-Jupiters¹ and very-hot-Jupiters² led to the conclusion that the evaporation of massive planets has to be modest.

In that frame the discovery that the transiting extrasolar planet HD 209458 b is indeed losing mass was mostly unexpected (Vidal-Madjar et al. 2003). From the observation of $15 \pm 4\%$ absorption in Lyman- α during the transit, a lower limit of the H I escape rate was estimated to be of the order of $\sim 10^{10} \text{ g s}^{-1}$ (Vidal-Madjar et al. 2003; Vidal-Madjar & Lecavelier des Etangs 2004). This mass loss rate corresponds to a loss of $\sim 0.1\%$ of the total mass of the planet over 10 billion years (10 Gyr). Models of the time variation of this escape rate lead to slightly larger values for the total fraction of mass loss over the whole stellar life (see e.g., Lecavelier des Etangs et al. 2004; Baraffe et al. 2004).

Different detailed models have been developed to understand the observed evaporation process and to estimate the escape rate (e.g., Yelle 2004; Tian et al. 2005, García

¹ usually defined as massive planets orbiting in less than 10 days

² usually defined as planets orbiting in less than 3 days (e.g., Gaudi et al. 2005)

Muñoz 2006), to be compared with the observational constraints (Vidal-Madjar et al. 2003, 2004). Finally, it has been suggested that evaporation can lead to significant modification of the planets nature in the case of planets with a mass only a fraction of the mass of the observed hot-Jupiter and orbiting close to their parent stars (Lecavelier des Etangs et al. 2004; Baraffe et al. 2005).

However, models were applied to specific cases; it is not yet possible to conclude on the order of magnitude of the possible evaporation of planets which are being discovered without the effort to model in detail each particular case. The purpose of the present paper is not to review previous works and extended modeling efforts. Here we propose an alternative approach to obtain general characteristics from basic observed parameters. This approach allow statistical conclusion without the need to model in detail every individual planet for which detailed physical characteristics are not available. We propose to outline the main characteristics of a given planet that allow concluding on the general trend of its evaporation status, escape rate and lifetime related to the erosion through evaporation.

Here we present the idea of an energy diagram to address these issues (Sect. 2), and the way to simply estimate the energetic characteristics of a given planet (Sect. 3 and 4). Then an evaluation of the lifetime and escape rates is presented in Sect. 5. The resulting diagram is shown in Sect. 6. A diagram corresponding to the escape rate is given in Sect. 7. Uncertainties and evolutionary tracks are presented in Sect. 8 and 9. Finally we conclude on the possible nature of the recently discovered Neptune mass planets (Sect. 10).

2. Potential energy of planets versus stellar energy flux

A plot of the lifetime of planets as function of their masses and orbital distances has been calculated by Lecavelier des Etangs et al. (2004). The purpose of this plot is to show that the identified planets are stable against evaporation. For the existing planets, the lifetime, defined as the time to escape the full mass of the planet, is always longer than $\sim 10^{10}$ years (Fig. 5 of Lecavelier des Etangs et al. 2004). Attempts have been made to extrapolate from this plot possible escape rate in the case of planets discovered later (HD 149026 b, Valenti 2005). It would be extremely valuable to have a quick diagnostics on the evaporation rate of a given planet to predict if there are any chances to observe and constrain the evaporation through, e.g., Lyman- α observation during a transit (Lecavelier des Etangs et al., in preparation). However, in the lifetime plot of Lecavelier des Etangs et al. (2004), the energy flux from the star is assumed to be the one of HD 209458 b. The energy flux from other stars is certainly different depending on the stellar type, rotation period, etc. The second critical parameter in this plot is the assumed planetary radii. In the lifetime plot of Lecavelier des Etangs et al. (2004), the radius of HD 209458 b (1.35 Jupiter radii) was used to normalize the scaling laws for the planetary

radii because at the time of this work HD 209458 b was the only hot-Jupiter whose radius had been measured. However, the radius of HD 209258 b is now considered as anomalously large (Guillot 2005; Lecavelier des Etangs & Vidal-Madjar 2006). From observations of ten transiting planets (Bouchy et al. 2005b, McCullough et al. 2006) and detailed modeling of the planetary structure (Guillot 2005), 1.1 Jupiter radii is certainly more appropriate for a 1 Jupiter mass planet close to its parent star. This makes HD 209458 b with its 1.35 Jupiter radii and 0.69 Jupiter mass clearly a peculiar object. In the following we will therefore use a fit to the Guillot's model. A new plot has been calculated with this new information (Lecavelier des Etangs & Vidal-Madjar 2006). However, the planetary radius depends also on parameters other than the planetary mass and orbital distance, for instance, the stellar type and the corresponding effective temperature of the central star and its age. It is thus impossible to uniquely estimate lifetime and escape rate from the position of a given planet in the orbital distance versus mass diagram. As a consequence, this plot has to be revisited.

In summary, since each planet has different radius and different energy flux entering onto the upper atmosphere from stars of different type, the orbital distance versus mass diagram is not appropriate to conclude on the escape rate and life time of a variety of planets. We have to define the parameters (or combination of parameters) which allow us to conclude on that matter.

After the realization that HD 209458 b is losing mass, many modeling efforts have been pursued to better understand the escape in the particular case of hot-Jupiters. The common results of these numerous models is that almost 100% of the EUV/Lyman- α energy flux which is converted into heat is then transferred into escape (see, for instance, Yelle 2004 and Tian et al. 2005). Even magnetic fields which can inhibit ion escape are found to have modest impact. Yelle (2004) found that the net escape rate with ion escape inhibited by magnetic field is only 30% smaller than in its reference model. Similarly, effects of dissociation and ionization of H_2 are found to be negligible. The resulting escape rates of these various models are different not because these models assumed different mechanisms but because of the different illumination, planetary cross section for the energy flux, and fraction of this energy converted into heat to the upper atmosphere.

As a result, the evaporation status of a set of different planets orbiting different stars can be obtained by a comparison of the energy deposited in the upper atmosphere and used to escape the planet gravity, *i.e.* to compensate for the (negative) potential energy of the atmospheric gas, with this potential energy. We therefore propose to calculate the position of the extrasolar planets in a diagram displaying the potential energy versus the stellar energy deposition. We now evaluate these two quantities in the two next sections to plot the corresponding diagrams in Sect. 6 and 7.

3. The extreme ultraviolet illumination from the central stars

The present and past illumination from the parent stars is a key parameter which needs to be accounted for. First, as the planet-hosting stars are cooler than early F stars in the main sequence, the stellar energy emitted in the near UV range is negligible (e.g., Kurucz 1993). Moreover, near UV and optical energy is absorbed deep in the bottom and dense atmosphere. On the contrary, neutral components of atmospheres have large cross section in the extreme ultraviolet ($100\text{\AA} < \lambda < 1200\text{\AA}$). Photons in the extreme ultraviolet wavelength range (EUV) are thus easily absorbed by the tenuous upper atmospheres of planets. For instance, in the terrestrial planets of the Solar system, the EUV energy flux is the main driver of the escape (e.g., Chamberlain & Hunten 1987). Therefore, for simplicity and in agreement with the result of all detailed models of the evaporation of hot-Jupiters, we can assume that the energy flux deposited in the upper atmosphere and transferred into escape energy mainly comes from the EUV.

However, because of the interstellar absorption, there are very few observational constraints on the EUV flux from the stars in the solar neighborhood. On the other hand, although stellar EUV fluxes are related to stellar rotational velocities (Wood et al. 1994), most of the stars harboring extrasolar planets have no published rotational velocities or only upper limits. In most cases, the information on the planet-hosting stars is limited to the stellar type. We have hence chosen to consider the very extreme ultraviolet luminosities L_{S2} as a function of the stellar type, as measured by *Rosat* in the S2 channel between 110 and 200 \AA . We then scale these luminosities to the solar EUV flux of $\sim 4.6 \text{ erg cm}^{-2} \text{ s}^{-1}$ at 1 AU as given by Ribas et al. (2005). This solar value is obtained considering mid-solar cycle data of 1993 as representative of the Sun at the average activity. The EUV flux, $F_{\text{EUV}}(1 \text{ AU})$, received by a planet by unit area at 1 AU is hence calculated using

$$F_{\text{EUV}}(1 \text{ AU}) = 4.6 \frac{L_{S2}}{L_{S2, \text{G stars}}} \text{ erg cm}^{-2} \text{ s}^{-1}. \quad (1)$$

The scale between L_{S2} luminosities and EUV is justified by the fact that both the $\sim 100 - 200 \text{\AA}$ and the extreme-far UV fluxes are emitted by the same region in the chromosphere and the transition region where the temperature is observed to increase from the photospheric to the coronal values.

Hodgkin and Pye (1994) give median S2 luminosities as a function of the spectral types, with value of $10^{27.9}$, $10^{26.8}$, $10^{27.3}$ and $10^{26.6} \text{ erg s}^{-1}$ for F, G, K and M stars respectively. Concerning the F type stars, most of the F stars known to harbor planets are late type F8V or F9V stars. Because early F stars remain chromospherically active and fast-rotating during their main sequence phase, the accuracy in the measurement of their radial velocity is strongly limited. It is yet impossible to detect planets around them (F. Pont, private communication). But these

early F stars contribute to the mean value of the observed S2 luminosities of the whole class of F stars. We therefore decided to consider a typical S2 luminosity of $10^{27.3} \text{ erg s}^{-1}$ for F6 and F7 stars harboring planets, and an S2 luminosity of $10^{26.8} \text{ erg s}^{-1}$ for later F8V and F9V stars which are more similar to G0V type stars.

Using these S2 luminosities and the solar EUV luminosity, we find $F_{\text{EUV}}(1 \text{ AU}) = 14.7, 4.6, 4.6, 14.7$ and $2.9 \text{ erg cm}^{-2} \text{ s}^{-1}$ for F6-F7, F8-F9, G, K, and M stars, respectively. Except if explicitly mentioned (Sect.8), these values will be used throughout the paper. These fluxes can be converted to the energy per unit of time, dE_{EUV}/dt , received by a planet of radius R_p with an orbital distance a_p using:

$$dE_{\text{EUV}}/dt = \pi R_p^2 \left(\frac{a_p}{1 \text{ AU}} \right)^{-2} F_{\text{EUV}}(1 \text{ AU}). \quad (2)$$

4. Potential energy

To evaluate the total lifetime of a planet in an energetic point of view, we need to consider the total potential energy, E_p , of the planet considered as a whole, from its surface to its deep interior. If this energy is given in *erg*, the ratio with the received energy expressed in *erg per billion of years* will provide an estimate of the total time needed to cancel the (negative) potential energy, in other words, the evaporation lifetime. On the other side, to evaluate the escape of the atmospheric gas at the present time, we need to consider the potential energy of the gas only in the atmosphere and per unit of mass. The ratio of this quantity with the energy received will provide the mass escape rate. We see that we have two different quantities which need to be estimated: the potential energy of the whole planet and the potential energy per unit of mass in the atmosphere

4.1. The potential energy of the whole planet

The potential energy of a gaseous sphere of radius R_p is given by

$$E_p = -G \int_0^{R_p} \frac{m(r)}{r} \frac{dm(r)}{dr} dr \quad (3)$$

where G is the gravitational constant and $m(r)$ is the mass inside a radius r . For a uniform density and a mass M_p , we obtain the classical formula $E_p = -3GM_p^2/5R_p$. But in general, the potential energy depends on the internal structure. For a planet with a mass M_p and a radius R_p , an analytical approximation can be found assuming a polytropic approximation of the equation of state for the planet interior. Using a polytropic index $n = 1$ ($P \propto \rho^2$, de Pater & Lissauer 2001) the potential energy is found to be:

$$E_p = -\frac{3}{4} GM_p^2 / R_p. \quad (4)$$

The details of the calculation are given in Appendix A. Numerically this converts into:

$$E_p = -2.9 \times 10^{43} \left(\frac{M_p}{M_{\text{Jup}}} \right)^2 \left(\frac{R_p}{R_{\text{Jup}}} \right)^{-1} \text{ erg}. \quad (5)$$

4.2. The potential energy per unit of mass in the atmosphere

Another interesting quantity is the potential energy of the atmospheric gas per unit of mass. This potential energy per unit of mass is simply given by (see Appendix B):

$$dE_{p(\text{atm})}/dm = -GM_p/R_p. \quad (6)$$

Numerically this converts into:

$$dE_{p(\text{atm})}/dm = -1.9 \times 10^{13} \left(\frac{M_p}{M_{\text{Jup}}} \right) \left(\frac{R_p}{R_{\text{Jup}}} \right)^{-1} \text{ erg g}^{-1}. \quad (7)$$

We note that the potential energy per unit of mass of the atmospheric gas is much higher than its kinetic or thermal energy, even if the gas is escaping at high velocity. For instance, even for gas escaping at high velocity of 10 km s^{-1} , the kinetic energy is $5 \times 10^{11} \text{ erg g}^{-1}$, which has to be compared with the typical value of $-dE_{p(\text{atm})}/dm \sim 10^{13} \text{ erg g}^{-1}$ for the known extrasolar planets (Sect. 7). Even for very-hot-Jupiters in which tidal forces indeed play a significant role (Sect. 4.3), the potential energy is expected to be always larger than the kinetic energy. The kinetic energy of the escaping gas is thus neglected in the present analysis.

4.3. Potential energy and tidal forces

In the case of hot-Jupiters and very-hot-Jupiters, the gravity from the nearby parent star modifies the geometry of the potential energy. In those cases, the iso-potentials around the planet at high altitude are no more spherical and are open to the infinity when the potential reaches the value of the Roche lobe. Therefore the energy needed to escape the planet can be defined by the energy needed to reach this Roche lobe. In the case of $M_p \ll M_*$, the potential energy of the atmospheric gas per unit of mass is accordingly modified by

$$dE'_{p(\text{atm})}/dm = dE_{p(\text{atm})}/dm + \Delta_{\text{tidal}} dE_{p(\text{atm})}/dm, \quad (8)$$

where (see Appendix B)

$$\Delta_{\text{tidal}} dE_{p(\text{atm})}/dm \approx \frac{3^{4/3}}{2} \frac{GM_*^{1/3} M_p^{2/3}}{a_p}, \quad (9)$$

a_p being the orbital distance of the planet and M_* the mass of the central star.

The potential energy of the whole planet as defined in Sect. 4.1 is also modified by tidal forces. We can define $\Delta_{\text{tidal}} E_p$ by

$$E'_p = E_p + \Delta_{\text{tidal}} E_p. \quad (10)$$

Fortunately, because Eq. 9 does not depend on the planetary radius, the change introduced by the tidal forces does not depend on the planet internal structure. Indeed, we have

$$\Delta_{\text{tidal}} E_p = \int_0^{R_p} \frac{3^{4/3}}{2} \frac{GM_*^{1/3} m(r)^{2/3}}{a_p} \frac{dm(r)}{dr} dr. \quad (11)$$

It is easy to find that for the total potential energy of a planet we have

$$\Delta_{\text{tidal}} E_p \approx \frac{3^{7/3}}{10} \frac{GM_*^{1/3} M_p^{5/3}}{a_p}. \quad (12)$$

Because $\Delta_{\text{tidal}} dE_{p(\text{atm})}/dm$ is positive, the energy deposition needed to escape the planet gravity is decreased by the tidal forces. For the identified hot-Jupiters, we find that the depth of their potential well is decreased by the tidal forces by typically 30 to 50%. For instance, we find that $\Delta_{\text{tidal}} dE_{p(\text{atm})}/|dE_{p(\text{atm})}| \sim 50\%$ for OGLE-TR-56b and $\sim 33\%$ for HD 209458 b. Keeping the hypothesis that the escape energy is mainly used to escape the potential well of the planet, this leads to a similar increase of the escape rate (Sect 5).

5. Lifetime and escape rate

Assuming that the energy deposited by the EUV flux is used to extract the gas which escapes the potential well of the planet with an efficiency $\epsilon = 1$, we can derive an escape rate, dm/dt , and a corresponding typical lifetime for a given planet. Assuming $-dE'_{p(\text{atm})} = \epsilon dE_{\text{EUV}}$, and neglecting the tidal forces ($dE'_{p(\text{atm})} \approx dE_{p(\text{atm})}$), we find:

$$dm/dt = -\frac{dE_{\text{EUV}}/dt}{dE_{p(\text{atm})}/dm}. \quad (13)$$

From Eq. 2, we derive the escape rate

$$dm/dt = F_{\text{EUV}}(1 \text{ AU}) \left(\frac{\pi R_p^3}{GM_p} \right) \left(\frac{a_p}{1 \text{ AU}} \right)^{-2}. \quad (14)$$

Numerically, this gives

$$dm/dt = 3.7 \times 10^7 \left(\frac{F_{\text{EUV}}(1 \text{ AU})}{4.6 \text{ erg cm}^{-2} \text{ s}^{-1}} \right) \times \left(\frac{R_p}{R_{\text{Jup}}} \right)^3 \left(\frac{M_p}{M_{\text{Jup}}} \right)^{-1} \left(\frac{a_p}{1 \text{ AU}} \right)^{-2} \text{ g s}^{-1}. \quad (15)$$

Concerning the lifetime, we can similarly assume $-E'_p = \epsilon \int_0^{t_1} dE_{\text{EUV}}$ to obtain a typical duration, t_1 , which corresponds to the time needed to fill the whole potential well of the planet assuming the current energy flux. This duration can hence be called a ‘‘lifetime’’; the nature of a planet can change through evaporation if t_1 is shorter than the typical lifetime of the parent star. If the energy received by the planet, dE_{EUV}/dt , is assumed to be constant over time, from the above equation we derive the lifetime t_1 :

$$t_1 = \frac{-E'_p}{dE_{\text{EUV}}/dt}. \quad (16)$$

However, when the planetary mass evolves, the radius and the corresponding energy flux captured by the planet changes, consequently also the real lifetime changes. A

more detailed analysis is possible by considering the variations of the escape rate as a function of time. This leads to a new “lifetime”, t_2 , which can be defined by

$$-E'_p = \left(\frac{a_p}{1 \text{ AU}}\right)^{-2} \int_{t_0}^{t_2} \pi R_p(t')^2 (F_{\text{EUV}}(1 \text{ AU})(t')) dt', \quad (17)$$

where t_0 is the initial time of the system. At this stage a useful quantity is the mean value of the EUV energy flux from the central star $\langle dE_{\text{EUV}}/dt \rangle$ defined by:

$$\langle dE_{\text{EUV}}/dt \rangle (t) \equiv \left(\frac{a_p}{1 \text{ AU}}\right)^{-2} \times \frac{\int_{t_0}^t \pi R_p(t')^2 (F_{\text{EUV}}(1 \text{ AU})(t')) dt'}{(t - t_0)}, \quad (18)$$

which includes the variations of the EUV flux and the variation of the planetary radius which both are larger during the early stage of the planetary system (Guinan & Ribas 2002; Ribas et al. 2005; Burrows et al. 2000). We can define a correction factor for time variation of the energy flux received by a planet,

$$\gamma \equiv \frac{\langle dE_{\text{EUV}}/dt \rangle}{dE_{\text{EUV}}/dt}. \quad (19)$$

Hence we have

$$t_2 \approx \gamma^{-1} t_1. \quad (20)$$

We now have to evaluate the impact of this γ correction factor. First, the variation of the EUV flux as a function of time has been thoroughly analyzed for G stars by Ribas et al. (2005) within the “Sun in time” program. A recent work reports similar results for K type stars (Lakatos et al. 2005). Roughly speaking, the EUV flux can be assumed to follow a power law in the form $F \propto t^{-\alpha}$, where α is close to 1. For G type stars, the 1-1200Å EUV flux is found to have $\alpha \sim 1.23$, while the Lyman- α has $\alpha = 0.72$ (Ribas et al. 2005). For K type stars, the stellar C IV emission lines, which are believed to emerge from the same coronal region as the EUV flux, follows a power law with $\alpha \sim 0.94$. We therefore can consider a power law with $\alpha = 1$ as a good approximation (see also Vardavas 2005). Assuming that the increase of the UV luminosities in the past has to be limited and should “saturate”, we consider that the luminosities do not vary at ages below 100 million years (Lakatos et al. 2005). With these values, and neglecting for the moment the variation of the planetary radius, we find that for $\alpha = 1.23$ we have $\gamma = 6.5$ at $t = 5$ Gyr, and for $\alpha = 0.75$ we have $\gamma = 4$. We can therefore consider a power law with $\alpha = 1$ as a good approximation.

The variation of the planetary radius is a more complex matter because this depends on the planetary characteristics like mass and orbital distance. Nonetheless, empirically we found that the published time variation of the planetary radius (Burrows et al. 2000, Guillot 2005) can be well fitted by a simple scaling law in the form :

$$R_p(t) = R_\infty + \beta t^{-0.3}. \quad (21)$$

We find good fits with $\beta = 0.2 R_\infty \text{ Gyr}^{0.3}$ for $M_p \gtrsim 0.3 M_{\text{Jup}}$, and with $\beta = 0.3 R_\infty \text{ Gyr}^{0.3}$ for $M_p \approx 0.1 M_{\text{Jup}}$.

Using $\alpha = 1$ for the power law of the luminosity variations and $\beta = 0.2 R_\infty \text{ Gyr}^{0.3}$ for the variation of the planetary radius, we find $\gamma = 6.8$ at $t = 2$ Gyr (the typical age of the F6-F7 stars harboring planets, Saffe et al. 2005) and $\gamma = 8.0$ at $t = 5$ Gyr (taken as the typical age of later type stars). Using for less massive planets $\beta = 0.3 R_\infty \text{ Gyr}^{0.3}$, we find $\gamma = 8.7$ at $t = 2$ Gyr and $\gamma = 10.0$ at $t = 5$ Gyr. In the following we consequently decided to consider $\gamma = 7$ for F6-F7 stars, and $\gamma = 8$ for later type stars.

If we consider that the EUV luminosities can be extrapolated with the t^{-1} function in the past earlier than at the age of 100 million years, down to the age of 30 million years, γ is then increased by about 25%. We thus conclude that the correction factor for time variation of the energy flux does not strongly depend on the epoch of this “saturation” of the EUV luminosities in the past.

6. The energy diagram

With the equations derived in the previous sections, we can now plot diagrams of the potential energy versus energy flux (Fig. 1). In particular Eqs. 4 and 12 are used to derive the potential energy, E'_p , and Eq. 18 (or a combination of Eqs. 2 and 19) is used to derive the mean EUV energy received per unit of time by the planets, $\langle dE_{\text{EUV}}/dt \rangle$. We used the characteristics of the 182 identified planets as tabulated by Schneider (2006) on June 15th, 2006.

The only remaining difficulty in the drawing of the plot lies in the mass determination. Except for the case of transiting planets (Sect. 8), most of the planets have only a determination of $M_p \sin i$, where i is the orbit inclination. We compensate for this effect by multiplying the $M_p \sin i$ by a factor $\sqrt{2}$. This $\sqrt{2}$ factor is taken because the real mass M_p is statistically smaller than $\sqrt{2} M_p \sin i$ in 50% of the cases, and larger in 50% of the cases. The result is thus a spread of the position of the planets in the energy diagram. For transiting planets because $\sin i \approx 1$, we keep the measured mass without applying a correction factor.

From these planetary masses and using the tabulated types of the parent stars we estimate the planetary radius by fitting the radius versus mass curves calculated by Guillot (2005). This model assumes a central rock core and a gaseous envelope following an hydrogen-helium equation of state with an helium mixing ratio $Y = 0.30$. The estimated radii should not be sensitive to the evaporation, because they result from a calculation of the planet interior at several bars pressure not affected by the evaporation operating much higher in the atmosphere; this is confirmed by the absence of correlation of the observed radii of transiting planets with age and EUV flux received during the planets’ lifetime (Guillot et al. 2006). An indetermination remains for the very low mass planets (Neptune mass planets) because their radius (or density) as a function of their mass strongly depends on their nature. As a first approach and to plot the energy diagram in Fig. 1,

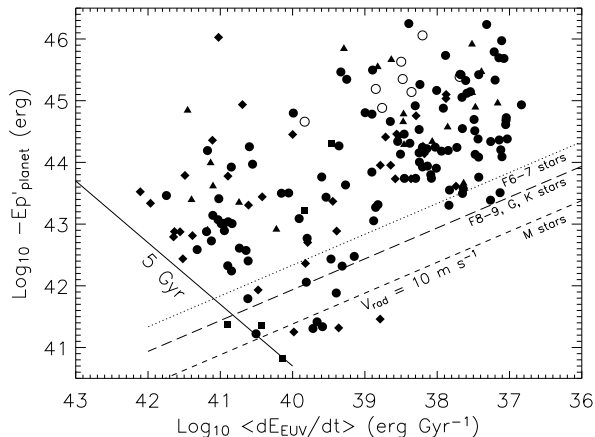


Fig. 1. Plot of the potential energy of the extrasolar planets as a function of the mean EUV energy received per billion of years, $\langle dE_{\text{EUV}}/dt \rangle$. To keep the planets with the smallest orbital distances in the left part of the diagram, the direction of the abscissa axis is chosen with the largest value of the mean energy flux toward the left. The 182 identified planets are plotted with symbols depending on the type of the central star: triangles for F stars, filled circles for G stars, diamonds for K stars and squares for M stars; planets orbiting class III stars are plotted with empty circles. The absence of planets in the bottom right region can be explained by the detection limit of the radial velocity surveys. There are indeed very few planets with radial velocities of the parent stars below the lines for which the radial velocity is 10 m s^{-1} . The radial velocity iso-curves at 10 m s^{-1} have been plotted for various stellar types (see Appendix C); the iso-curves for F8-F9, G and K-type stars are found to be nearly superimposed and are plotted with a single line.

The striking result is the absence of planets in the bottom left region which corresponds to light planets (small $-E'_p$) at short orbital distances (large $\langle dE_{\text{EUV}}/dt \rangle$). A plot of the lifetime line at $t_2=5 \text{ Gyr}$, shows that there are no planets in this part of the diagram simply because this is an evaporation-forbidden region. Planets in this region would receive more EUV energy than needed to fill the potential well of the planet, and evaporate in less than 5 Gyr.

we consider that these planets have a typical density of 2 g cm^{-3} for 15 Earth mass and 6 g cm^{-3} for 6 Earth mass. A detailed analysis of these planets in this diagram will be presented in Sect. 10.

The first plot (Fig.1) shows the total potential energy of the planet as a function of the mean energy flux $\langle dE_{\text{EUV}}/dt \rangle$. We decided to plot the mean energy flux on the abscissa axis in reverse order with larger values in the left. This choice is done to keep the planets with short orbital distances in the left part of the diagram for consistency with previous plots like, for instance, the diagram of Lecavelier des Etangs et al. (2004). The opposite of the

potential energy, $-E'_p$, is larger for more massive planets, and massive planets are therefore found in the upper part of the diagram. In some way this diagram is close to the classical diagram of mass versus orbital distance. However, in the present diagram the position reflects the impact of the evaporation on the planetary nature.

We plot the diagram with the 182 identified extrasolar planets. The striking result is the absence of planets in two different regions of the diagram. The absence of planets in the bottom right region can be explained by the detection limit of the radial velocity surveys. We plotted the limit for radial velocity of 10 m s^{-1} . As expected, we see that very few planets have radial velocities of the parent stars below this limit.

The most important region devoid of planets in the diagram is the bottom left region. This region should contain light planets at short orbital distances. However a plot of the lifetime line at $t_2=5 \text{ Gyr}$, shows that there are no planets in this part of the diagram simply because this is an evaporation-forbidden region. Planets in this region would receive more EUV energy than needed to fill the potential well of the planet and evaporate the gas, leaving a remaining core, an evaporation remnant (also named a “chthonian” planet; Lecavelier des Etangs et al. 2004).

From the position in the diagram, the typical lifetime of a given planet can be rapidly extracted. If the mean energy flux $\langle dE_{\text{EUV}}/dt \rangle$ is given in unit of *erg per billion years*, and the potential energy is given in unit of *erg*, the simple ratio of both quantities provides the corresponding lifetime in billion of years. In the diagram, lifetime isochrones are straight lines. In the Fig. 1, we plotted the line corresponding to the lifetime of 5 Gyr.

7. Diagram of the potential energy of the atmosphere and the corresponding escape rate

With the above equations (Eqs. 2, 6 and 9) we can also plot the potential energy per unit mass of the atmosphere as a function of the present time energy flux (Fig. 2). We again superimposed the position of the 182 identified planets.

Although apparently similar to the previous diagram, this new diagram allows the estimate of the actual evaporation rate for a given planet, assuming that most of the energy in the extreme ultraviolet is used to escape the combined effect of planet gravity and tidal forces. In Fig. 1, we considered the total potential energy providing a hint on the total escape mass and time. Here in Fig. 2, we consider the potential energy *per unit of mass* (erg g^{-1}) of the atmospheric gas versus the *present* time input energy (erg s^{-1}). The ratio of both quantities provides a hint of the present escape *rate* (g s^{-1}).

We see in the plot that the extrasolar planets must have escape rate in the range 10^5 to 10^{12} g s^{-1} . The largest escape rates are obtained for OGLE-TR-113 b, HD 189733 b, HD 46375 b, HD 63454 b, and TrES-1, for which we obtain escape rates of 3.5×10^{11} , 3.2×10^{11} , 2.8×10^{11} , 2.5×10^{11} , and $2.2 \times 10^{11} \text{ g s}^{-1}$, respectively.

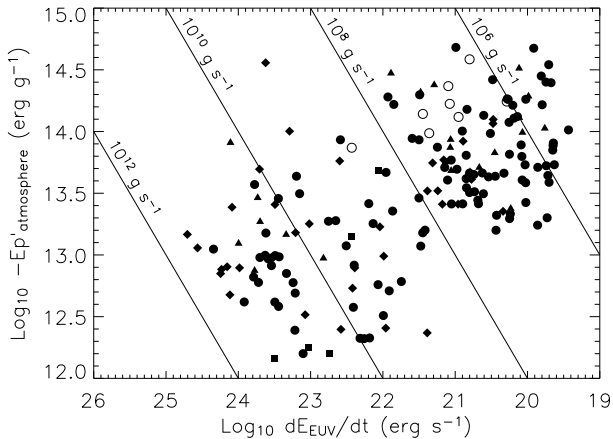


Fig. 2. Plot of the potential energy per unit of mass of the atmosphere of the extrasolar planets as a function of the EUV input flux. Unlike Fig. 1, the potential energy is per unit of mass at one planetary radius in erg g^{-1} ; and the EUV input flux is the value at the present time in erg s^{-1} . This allows to directly estimate the corresponding escape rate at the present time in g s^{-1} . The escape rates are drawn with straight lines for 10^6 , 10^8 , 10^{10} and 10^{12} g s^{-1} . The 182 identified planets are plotted with the same symbols as in Fig. 1.

These five stars are cataloged as K type stars and therefore assumed to have large extreme ultraviolet luminosities. The next largest escape rate is found for an M type star, GJ 436 b, for which we estimate a maximum escape rate of the order of $2.2 \times 10^{11} \text{ g s}^{-1}$.

For HD 209458 b, we obtain an escape rate of $9 \times 10^{10} \text{ g s}^{-1}$, which is consistent with the lower limit of $\sim 10^{10} \text{ g s}^{-1}$ obtained from the interpretation of the Lyman- α transit light curve (Vidal-Madjar et al. 2003; Vidal-Madjar & Lecavelier des Etangs 2004).

8. Uncertainties

For the observed planets, the position in the previous diagrams are obtained by simple estimates of the EUV luminosities and planetary radii. These rough estimates are subject to uncertainties. These uncertainties add some dispersion in the clouds of points of a given diagram; however with a limited dispersion, this does not severely affect the main trends and the corresponding statistical conclusions, like the empty region observed for lifetime below 5 Gyr. More critically, when we consider a particular planet, we need to have an estimate of the uncertainties introduced by above approximations.

To evaluate the impact of these approximations on the planetary radius and stellar EUV luminosities, we used the transiting planets. For these planets, we have a measured radius and also a better estimate of the EUV luminosities through the rotational velocity of the central stars $v \sin i$ (when measured, in few cases only upper limits are

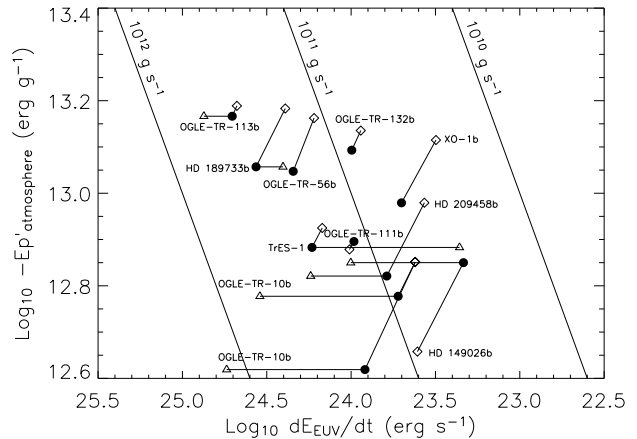


Fig. 3. Plot of the potential energy per unit of mass of the atmosphere of the ten *transiting* planets as a function of the EUV input flux. For each planet the position is calculated using the radius as modeled (diamonds) and the radius as effectively measured (circles). For OGLE-TR-10b we used the two possible planetary radii quoted by Santos et al. 2006. When available, the EUV luminosities estimated from the stellar rotational velocity are plotted with triangles.

available). Because the rotational axis of the stars is expected to be close to the orbital axis of the planets (see for instance Queloz et al. 2000), and for transiting planets $\sin i \simeq 1$, the measured $v \sin i$ are in fact true rotational velocities from which better estimates of the EUV luminosities can be obtained. We plotted these transiting planets in the diagram of the potential energy per unit of mass versus EUV energy flux (Fig. 3).

Concerning the radius estimate, OGLE-TR-10b is a special case because this planets has presently two different radius estimates which are significantly different. From the analysis of Bouchy et al. 2005a, Santos et al. 2006 obtain a radius of 1.43 Jupiter radii, while they obtain a radius of 1.14 Jupiter radii using the new observational data of Holman et al. 2005. Because we cannot discriminate between both results, we decided to keep both radii in the present discussion.

We first evaluate the uncertainty on the radius estimate and its impact on the evaporation rate. Because $dE_p(\text{atm})/dm \propto R_p^{-1}$ and $dE_{\text{EUV}}/dt \propto R_p^2$, the resulting escape rate dm/dt is quite sensitive to the planetary radius and is proportional to R_p^3 . For each planet in Fig. 3, we consider the radius obtained from our fit to Guillot's models (Guillot 2005; plotted with diamonds) and the radius as effectively measured (plotted with filled circles). In the ten transiting planets the difference between the two corresponding escape rates has a mean value of 0.13 dex and a dispersion of 0.22 dex. The largest differences are obtained for OGLE-TR-10 (increase of the escape rate by 0.45 dex with the radius given by Bouchy et al. 2005a), HD 209458 b (increase of the escape rate by 0.33 dex with

the real radius) and HD 149026 b (decrease of the escape rate by 0.41 dex with the real radius). This is due to the unexplained excess of planetary radius of OGLE-TR-10 and HD 209458 b (Guillot et al. 2005, Laughlin et al. 2005) and the small radius of HD 189733 b explained by its large metallicity and its suspected massive core (Sato et al. 2005). To conclude, although the escape rate is quite sensitive to the radius estimate calculated from the planet characteristics, the transiting planets allows us to estimate that this leads to a typical uncertainty of less than 0.3 dex in the calculated escape rate.

The impact of the EUV energy flux estimate is more difficult to constrain as we do not have real EUV flux measured for any of the stars harboring planets. However, we can use another estimate of the EUV luminosities through true rotational velocity when available in the published literature (*i.e.* for six of the ten transiting planets). For these six planets we calculated the EUV luminosities from their rotational velocity using the results of Wood et al. (1994). Using *Rosat* S2 measurements of stars within 10 parsecs Wood et al. (1994) found a close correlation between the S2 luminosity, L_{S2} , and the stellar rotational velocity, v_{rot} : $L_{S2} \propto v_{\text{rot}}^{1.4}$. From this equation, and assuming $F_{\text{EUV}} = 4.6 \text{ erg cm}^{-2} \text{ s}^{-1}$ at 1 AU and $v_{\text{rot}} = 2.0 \text{ km s}^{-1}$ for the Sun, we find an EUV energy flux of:

$$F_{\text{EUV}}(1 \text{ AU}) = 4.6 \left(\frac{v_{\text{rot}}}{2.0 \text{ km s}^{-1}} \right)^{1.4} \text{ erg cm}^{-2} \text{ s}^{-1} \quad (22)$$

at a distance of 1 AU from a star with a rotational velocity v_{rot} .

For the six transiting planets with published rotational velocity we plot the result in Fig. 3 with triangles. In these six planets the difference between the two corresponding escape rates has a mean value of 0.18 dex and a dispersion of 0.60 dex. The biggest differences are obtained for OGLE-TR-10 (increase of the escape rate by 0.82 dex with the EUV luminosity estimated from the rotational velocity) and TrES-1 (decrease of the escape rate by 0.87 dex). This is due to the large rotational velocity of OGLE-TR-10 with $v \sin i = 7.7 \text{ km s}^{-1}$ (Bouchy et al. 2005a), and the small rotational velocity of TrES-1 with $v \sin i = 1.08 \text{ km s}^{-1}$ (Laughlin et al. 2005). As a result, we see that in two of the six cases, we have a large uncertainty of the EUV luminosity with consequently a relatively large uncertainty in the escape rate (~ 0.8 dex), for the four other cases the dispersion is reduced to 0.4 dex. In general, taken into account the two uncertainties (radius and energy flux estimates), we find that the differences in the estimated escape rates have a typical dispersion of 0.7 dex.

9. Evolution tracks

The diagram described above aims at describing the possibility of the planets evolution on billion years time scale through the evaporation process. The position in the diagram can be calculated or evaluated at a given time, in

particular in the present epoch (assuming an age for the parent star). It is thus interesting to see how a planet can evolve in such a diagram. An interesting aspect of the diagram is that the position in the diagram in itself contains the information of the evolution timescale.

We thus calculated evolution tracks for few cases of planets for which the initial conditions imply rapid evolution through evaporation. This concerns light planets at short distances (Saturn mass planets at very-hot-Jupiter distances). In calculating these evolution tracks, the critical parameter is found to be the planetary radius and mass at a given age, both evolving with time. Again we assumed that the EUV flux varies as t^{-1} and used our fit to the Guillot et al. models and the corresponding time evolution described by Eq. 21. The result is plotted in Fig. 4.

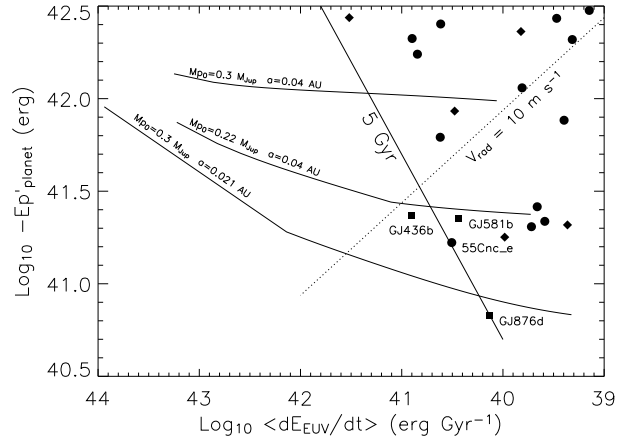


Fig. 4. Plot of the potential energy of the extrasolar planets as a function of the EUV input flux with evolutionary tracks superimposed. This is an enlargement of Fig 1. Time evolution of planets at constant orbital distance $a_p = 0.021 \text{ AU}$ and $a_p = 0.04 \text{ AU}$, corresponding to the orbital distances of GJ 876 d and two Neptune-mass planets (GJ 581 b and 55 Cnc e), respectively. GJ 581 b and 55 Cnc e are on the track of a planet with an initial mass $M_p(t_0) = 0.22 M_{\text{Jup}}$. GJ 876 d is on the track of a planet with an initial mass of $M_p(t_0) \sim 0.3 M_{\text{Jup}}$, showing that it can be the remnant of a former hot Saturn-mass planet.

We calculated the time evolution of planets at orbital distance $a_p = 0.021 \text{ AU}$ and $a_p = 0.04 \text{ AU}$, corresponding to the orbital distances of GJ 876 d and two Neptune-mass planets (GJ 581 b and 55 Cnc e), respectively. We find that GJ 581 b and 55 Cnc e can well be the remnant of a planet with an initial mass of $0.22 M_{\text{Jup}}$. The evolution track of a planet with an orbital distance of 0.021 AU and an initial mass of $0.3 M_{\text{Jup}}$ shows that GJ 876 d can be the remnant of a planet whose initial mass could be up to the mass of Saturn.

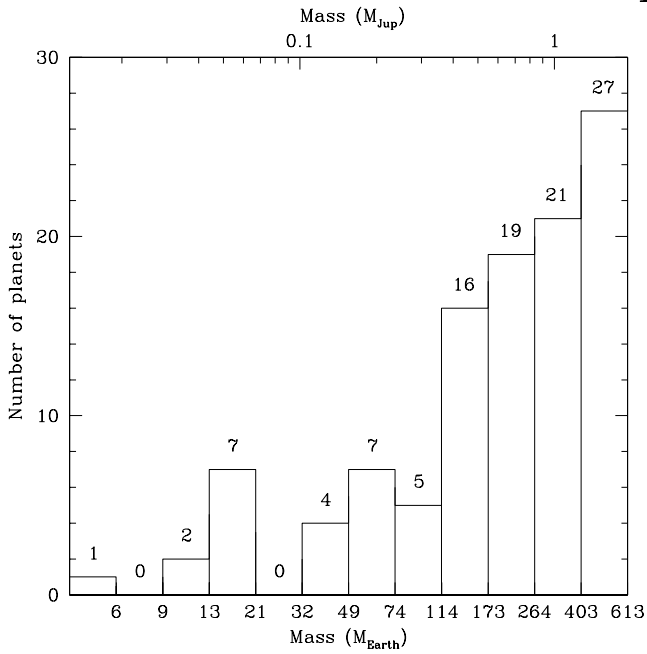


Fig. 5. Mass distribution of planets discovered through radial velocity.

10. Neptune mass planets in the diagram

A plot of the mass distribution of the extrasolar planets shows that Neptune mass planets play a particular role (Fig. 5). Ten planets have been found with mass below $0.067 M_{\text{Jup}}$ (21 Earth-mass), while no planets have been identified with mass between $0.067 M_{\text{Jup}}$ and $0.11 M_{\text{Jup}}$ (35 Earth-mass). The presence of this gap is not related to a bias in the radial velocity searches, since more massive planets are easier to detect (at the same orbital distances). This reveals the different nature of these Neptune mass planets orbiting at short orbital distances. But their nature is still a matter of debate (Baraffe et al. 2005). In particular the question arises if they can be the remnants of evaporated more massive planets (“chthonian planets”) as foreseen in Lecavelier des Etangs et al. (2004) ? Other possibilities include gaseous Neptune-like planets, super-Earth (Santos et al. 2004) or ocean-planets (Kutchnner 2003, Léger et al. 2004).

The mass of these objects being measured, the freedom for their position in the energy diagram mainly relies on the determination of their radius, or, in other words, of their mean density, *i.e.*, their nature. As a first approach, in Fig. 1 we considered that these planets have a typical density of 2 g cm^{-3} for 15 Earth mass and 6 g cm^{-3} for 6 Earth mass. Now we can test the density hypothesis and try to conclude on the possible nature of these planets. We plotted the position of these Neptune mass planets in the energy diagram with different hypothesis on their density (Fig. 6). We used mean planetary density of $\rho_p = 6 \text{ g cm}^{-3}$ for a typical density of refractory-rich planets which should describe the chthonian and super-Earth planets. A lower density on the order of $\rho_p = 2 \text{ g cm}^{-3}$

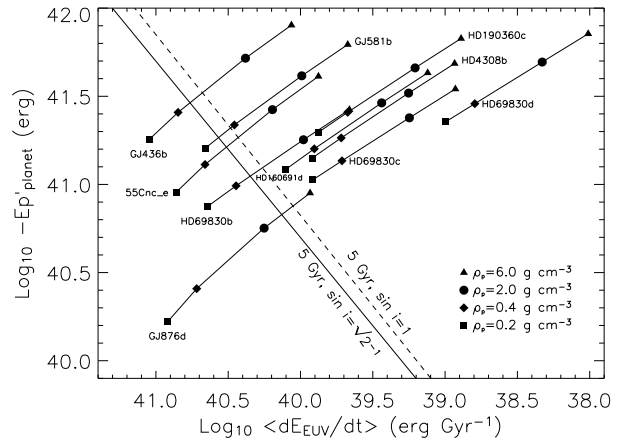


Fig. 6. Plot of the potential energy of the Neptune mass planet as a function of the EUV flux for various planets’ density. For GJ 581 b, GJ 436 b, HD 69830 b, 55 Cnc e and GJ 876 d, and assuming $\sin i = \sqrt{2}-1$, lifetime shorter than 5 Gyr are obtained for densities below 0.28, 0.55, 0.56, 0.69 and 3.1 g cm^{-3} , respectively. If $\sin i = 1$ (dotted line), the critical (minimum) densities are increased to 0.38, 0.74, 0.78, 0.93 and 4.2 g cm^{-3} , for GJ 581 b, GJ 436 b, HD 69830 b, 55 Cnc e, and GJ 876 respectively.

can be considered as more plausible for volatile-rich planets describing the ocean planets. For gas-rich planets we assumed much lower density of $\rho_p = 0.2 \text{ g cm}^{-3}$ and $\rho_p = 0.4 \text{ g cm}^{-3}$, describing planets which should look more like irradiated Neptune-like planets (Baraffe et al. 2006 find densities of 0.1 to 0.25 g cm^{-3} for the final stage of an evaporated gaseous planets with a 6 Earth mass core and final mass of about one Neptune mass).

In the energy diagram, HD 190360 c, HD 4308 b, HD 160691 d, HD 69830 c and HD 69830 d are all located in the possible domain with lifetime above 5 Gyr, independently of their assumed density. Even with very low densities down to 0.2 g cm^{-3} , these planets do not receive enough energy from their central star to evaporate significantly. For GJ 581 b only the extreme case $\rho_p = 0.2 \text{ g cm}^{-3}$ is in the evaporation-forbidden region. Owing to their orbital distances between 0.09 and 0.63 AU, it appears that the evaporation is not efficient enough to modify the nature if these planets. These planet are not likely to be the evaporation remnants of previously more massive planets

For GJ 436 b, 55 Cnc e and HD 69830 b, density below 0.4 g cm^{-3} would place these planets in the evaporation-forbidden region of the energy diagram. If these planets were formerly low density (gaseous giant) planets, they must have lost a large fraction of their upper atmospheric gas. We therefore conclude that, with low orbital distances in the range 0.03 to 0.08 AU, these planets cannot belong to the category of low mass gaseous planet (irradiated Neptune-like planets). The position of these planets in the energy diagram shows that they must contain a large fraction of solid/liquid material in the form of volatile or

refractory elements. These planets can be the remnants of previously more massive planets (chthonian planets) or alternatively volatile-rich planets (ocean planets) or rocky planets (super-Earths).

It is noteworthy that the conclusion for HD 69830 b is consistent with the one reached by Lovis et al. (2006) who concluded from formation and migration models that it must have a mainly rocky composition.

For GJ 876 d, even the density of an ocean planet creates some problem. GJ 876 d needs to be a planet dense enough to be located above the $t_2 = 5$ Gyr lifetime limit. This planet requires a density larger than 3.1 g cm^{-3} for its atmosphere to survive. GJ 876 d could be a big rocky planet, like a super-Earth, or a refractory remnant of a previous more massive planet (an evaporated ocean planet?). However, we note that its parent star is an M star, and we have very little information about the EUV flux of non active M dwarfs; even if every M star has period of strong activity remains unclear. A more detailed analysis of the energy flux from this star and its possible consequences on this intriguing planet is needed.

In brief, the energy diagram allows us to trace three different categories for the ten presently identified Neptune mass planets. For six of them, the EUV input energy seems not strong enough to affect significantly these planets; we cannot conclude on their nature. For three other planets, it appears that they cannot be a kind of low mass gaseous planets. These planets must contain a large fraction of solid/liquid material. Finally, GJ 876 d must be dense enough to survive the strong EUV energy flux from its nearby parent star. This planet must contain a large fraction of massive elements.

11. Conclusion

To describe the evaporation status of the extrasolar planets, we proposed to consider an energy diagram in which the potential energy of the planets is plotted versus the energy received by the upper atmosphere. We presented a basic method to estimate these quantities. For the energy flux, we proposed a first approach using the type of the parent stars or, if available, their rotation period. For the potential energy, we included the modification of the gravity field by the tidal forces from the parent stars. This description allows a quick estimate of both the escape rate of the atmospheric gas and the lifetime of a planet against the evaporation process. We found that the region of lifetime below 5 Gyr is devoid of planets, which reinforces the belief that this diagram is an appropriate description of the evaporation. In the evaporation-forbidden region, the evaporation can modify the nature and the characteristics of the planets such that they move to region of the diagram corresponding to longer lifetime and consequently become long-lived.

The escape rates estimated from the diagram are found to be in the range 10^5 g s^{-1} to 10^{12} g s^{-1} , with few cases above 10^{11} g s^{-1} . Although this is a crude estimate, the estimated escape rate for HD 209458 b is found to be con-

sistent with the lower limit of 10^{10} g s^{-1} obtained from interpretation of the H I Lyman- α observations.

Finally, this diagram allows the description of the possible nature of the recently discovered Neptune-mass planets. We found that GJ 436 b, 55 Cnc e and HD 69830 b cannot be low mass gaseous planets. These planets must contain a large fraction of solid/liquid material. Concerning GJ 876 d, we argued that it must be dense enough to survive the strong EUV energy flux from its nearby parent star. GJ 876 d must contain a large fraction of massive elements.

Acknowledgements. This work has been motivated by many discussions with various people. In particular, I am extremely grateful to F. Bouchy, G. Hébrard, J. McConnell, F. Pont, G. Tinetti and A. Vidal-Madjar. I warmly thank the anonymous referee for his detailed comments which helped to clarify the paper. I thank the International Space Science Institute (ISSI) in Berne, Switzerland, for support and discussion during the workshop on transiting extrasolar planets.

Appendix A: The potential energy of a gaseous planet

The potential energy of a gaseous sphere of radius R_p is given by

$$E_p = -G \int_0^{R_p} \frac{m(r)}{r} \frac{dm(r)}{dr} dr \quad (\text{A.1})$$

where G is the gravitational constant and $m(r)$ is the mass inside a radius r . The internal structure, characterized by $m(r)$, is given by

$$\frac{dP}{dr} = -\rho(r) \frac{Gm(r)}{r^2}, \quad (\text{A.2})$$

where $\rho(r)$ is the density given by

$$\frac{dm}{dr} = 4\pi r^2 \rho(r), \quad (\text{A.3})$$

and the relation between the pressure $P(r)$ and the density $\rho(r)$ is given by the equation of state. An analytical solution can be found if we assume that the equation of state follows a polytropic with an index $n = 1$, which is found to be a good approximation for the gaseous planets interior (de Pater & Lissauer 2001). In that case, the equation of state is

$$P = K\rho^2, \quad (\text{A.4})$$

where K is a constant. The equations A.2, A.3 and A.4 can be analytically solved. This gives the density profile within the planet (de Pater & Lissauer 2001):

$$\rho(r) = \rho_c \left(\frac{\sin(C_K r)}{C_K r} \right), \quad (\text{A.5})$$

with

$$C_K = \frac{\pi}{R_p} = \sqrt{\frac{2\pi G}{K}}. \quad (\text{A.6})$$

Putting Eq. A.5 into Eq. A.1, this gives

$$E_p = -\frac{12G\pi^3\rho_c^2}{C_K^5}. \quad (\text{A.7})$$

Also using Eqs. A.3, A.5 and A.6, the planet mass, M_p is given by

$$M_p = m(R_p) = m(\pi/C_K) = \frac{4\pi^2\rho_c}{C_K^3}. \quad (\text{A.8})$$

Finally, putting Eq. A.6 and A.8 into A.7 we find the potential energy of a gaseous sphere in which the equation of state follows a polytropic with an index $n = 1$:

$$E_p = -\frac{3}{4}GM_p^2/R_p. \quad (\text{A.9})$$

Appendix B: Modification of the potential energy by tidal forces

In the field of a planet of mass M_p , at a distance r from the planet center, the potential energy field, χ , follows the equation

$$\chi(r) = -\frac{GM_p}{r} + C, \quad (\text{B.1})$$

where G is the gravitational constant and C is a constant. The potential energy of a unit mass of the atmospheric gas of a planet, $dE_{p(\text{atm})}/dm$, can be defined by the opposite of the energy needed to escape the planet gravity, in other words to reach infinite distance from the planet:

$$dE_{p(\text{atm})}/dm \equiv \chi(R_p) - \chi(\infty) = -GM_p/R_p. \quad (\text{B.2})$$

where R_p is the radius of the planet. This demonstrates the well known Eq. 6 given in Sect. 4.2.

However, in a star-planet system, the potential energy field is modified by the star gravity and centrifugal forces. Along the star-planet axis, the potential energy field, χ' , follows the equation:

$$\begin{aligned} \chi'(r) &= \chi(r) + \Delta\chi(r) \\ &= -G(M_p + M_*) \left[\frac{\mu}{r} + \frac{1-\mu}{a_p - r} + \frac{[(1-\mu)a_p - r]^2}{2a_p^3} \right] \\ &\quad + C, \end{aligned} \quad (\text{B.3})$$

where r is the distance from the planet center in the direction of the star on the star-planet axis, a_p is the star-planet distance, M_* is the stellar mass and μ is defined by

$$\mu = \frac{M_p}{M_p + M_*}. \quad (\text{B.4})$$

In the case $r \ll a_p$ and $\mu \ll 1$, we can derive

$$\frac{\Delta\chi(r)}{G(M_p + M_*)} = -\frac{3}{2a_p} \left(1 + \frac{r^2}{a_p^2} + O\left(\frac{r^3}{a_p^3}\right) + O(\mu) \right) + C. \quad (\text{B.5})$$

In the modified gravity field, the energy needed to escape the planet can be defined by the energy needed to reach

the Roche lobe. Along the star-planet axis, the Roche lobe is located at a distance $r = r_{\text{Roche}}$, where r_{Roche} follows:

$$\frac{\partial\chi'}{\partial r}(r_{\text{Roche}}) = 0. \quad (\text{B.6})$$

Again assuming that $r \ll a_p$, and using Eq. B.3 and B.6 we find

$$\mu = 3 \left(\frac{r_{\text{Roche}}}{a_p} \right)^3 + O\left(\frac{r_{\text{Roche}}}{a_p}\right)^4, \quad (\text{B.7})$$

from which we derive

$$\frac{r_{\text{Roche}}}{a_p} \approx \left(\frac{\mu}{3} \right)^{1/3}. \quad (\text{B.8})$$

Finally, the new potential energy of a unit mass of the atmospheric gas of a planet, $dE'_{p(\text{atm})}/dm$, defined by the opposite of the energy needed to escape the planet gravity, is now the energy to reach the Roche lobe:

$$\begin{aligned} dE'_{p(\text{atm})}/dm &\equiv \chi'(R_p) - \chi'(r_{\text{Roche}}) \\ &= [\chi(R_p) - \chi(r_{\text{Roche}})] \\ &\quad + [\Delta\chi(R_p) - \Delta\chi(r_{\text{Roche}})]. \end{aligned} \quad (\text{B.9})$$

In the case $\mu \ll 1$ and $R_p \ll a_p$, using Eq. B.1 and B.7 we derive for the first term of Eq. B.9:

$$\begin{aligned} \frac{\chi(R_p) - \chi(r_{\text{Roche}})}{G(M_p + M_*)} &= \\ &= -\frac{\mu}{R_p} + \frac{3}{a_p} \left(\frac{r_{\text{Roche}}}{a_p} \right)^2 + \frac{1}{a_p} O\left(\frac{r_{\text{Roche}}}{a_p}\right)^3. \end{aligned} \quad (\text{B.10})$$

For the second term of Eq. B.9, using Eq. B.5 we derive:

$$\begin{aligned} \frac{\Delta\chi(R_p) - \Delta\chi(r_{\text{Roche}})}{G(M_p + M_*)} &= \\ &= \frac{3}{2a_p} \left(\frac{r_{\text{Roche}}}{a_p} \right)^2 + \\ &= \frac{1}{a_p} \left(O\left(\frac{R_p}{a_p}\right)^2 + O\left(\frac{r_{\text{Roche}}}{a_p}\right)^3 + O(\mu) \right). \end{aligned} \quad (\text{B.11})$$

Here we implicitly assumed $(r_{\text{Roche}}/R_p)^2 \gg 1$, which is valid as the smallest values in extreme cases of very-hot-Jupiters are always larger than 10.

As a result, combining Eq. B.2, B.9, B.10 and B.11 we find

$$\begin{aligned} dE'_{p(\text{atm})}/dm &\approx dE_{p(\text{atm})}/dm \\ &\quad + \frac{9G(M_p + M_*)}{2a_p} \left(\frac{r_{\text{Roche}}}{a_p} \right)^2. \end{aligned} \quad (\text{B.12})$$

If we define $\Delta_{\text{tidal}}dE_{p(\text{atm})}/dm$ by

$$dE'_{p(\text{atm})}/dm \equiv dE_{p(\text{atm})}/dm + \Delta_{\text{tidal}}dE_{p(\text{atm})}/dm, \quad (\text{B.13})$$

using Eq. B.8 and B.12, we find

$$\Delta_{\text{tidal}}dE_{p(\text{atm})}/dm \approx \frac{3^{4/3}G(M_p + M_*)\mu^{2/3}}{2a_p}. \quad (\text{B.14})$$

That is

$$\Delta_{\text{tidal}} dE_{p(\text{atm})}/dm \approx \frac{3^{4/3}}{2} \frac{GM_*^{1/3} M_p^{2/3}}{a_p}. \quad (\text{B.15})$$

This result is obtained using the potential description in the direction of the star on the star-planet axis, but it is valid in all direction because the potential is the same on the whole Roche lobe surface which is defined as an isopotential. Therefore the energy needed to reach the Roche lobe and to escape the planet is the same in all directions.

Appendix C: The radial velocity iso-curves in the energy diagram

Most of the known planets have been detected with the radial velocity method which is not sensitive to low mass planets with large orbital distances. Therefore, if the detected planets are plotted in the energy diagram (Fig. 1), the absence of planets with small absolute value of the potential energy (low mass) receiving a low EUV energy (large orbital distance) is due to this bias of the radial velocity method. The amplitude of the radial velocity of a planet-hosting star, V_{rad} , is given by

$$V_{\text{rad}}^2 = \frac{GM_p^2}{a_p M_*}, \quad (\text{C.1})$$

where G is the gravitational constant, a_p the planet orbital distance, M_p and M_* are the mass of the planet and the star, respectively. Using Eq. 4, and the fact that

$$\frac{dE_{\text{EUV}}/dt}{P_{*,\text{EUV}}} = \frac{R_p^2}{4a_p^2}, \quad (\text{C.2})$$

where $P_{*,\text{EUV}}$ is the total power emitted in EUV by the parent star, we derive

$$E_p \approx -\frac{3}{8} M_* V_{\text{rad}}^2 \sqrt{\left(\frac{dE_{\text{EUV}}/dt}{P_{*,\text{EUV}}}\right)^{-1}}. \quad (\text{C.3})$$

This equation does not depend on the planetary radius, mass and orbital distance. Therefore, for a given stellar type, corresponding to a given stellar mass and total power emitted in the EUV, the radial velocity iso-curves must follow a straight line in the log-log energy diagram of E_p as a function of dE_{EUV}/dt .

Most of the instruments have a detection threshold at about 10 m s^{-1} . Instruments with larger sensitivity (like the *Harps* spectrograph) are recent and allowed the discovery of low mass planets only with short orbital periods. This explains why the detected planets below the limit at 10 m s^{-1} are in the left part of the energy diagram plotted in Fig. 1.

References

Baraffe, I., Selsis, F., Chabrier, G., et al. 2004, A&A, 419, L13
 Baraffe, I., Chabrier, G., Barman, T. S., et al. 2005, A&A, 436, L47

Baraffe, I., Alibert, Y., Chabrier, G., & Benz, W. 2006, A&A, in press (astro-ph/0512091)
 Bouchy, F., Pont, F., Melo, C., et al. 2005, A&A, 431, 1105
 Bouchy, F., Udry, S., Mayor, M., et al. 2005, A&A, 444, L15
 Burrows, A., & Lunine, J. 1995, Nature, 378, 333
 Burrows, A., Guillot, T., Hubbard, W. B., et al. 2000, ApJ, 534, L97
 Chamberlain, J. W. & Hunten, D. M. 1987, in *Theory of planetary atmospheres*, (Orlando, Acad. Press), Internat. Geophys. Ser., 36
 García Muñoz, A. 2006, Icarus Submitted
 Gaudi, B. S., Seager, S., Mallen-Ornelas, G. 2005, ApJ, 623, 472
 Guillot, T. 2005, Annual Review of Earth and Planetary Sciences, 33, 493
 Guillot, T., Burrows, A., Hubbard, W. B., Lunine, J. I., & Saumon, D. 1996, ApJ, 459, L35
 Guillot, T., Santos, N.C., Pont, F., et al. 2006, A&A, in press, astro-ph/0605751
 Guinan, E. F., Ribas, I., Harper, G. M., & Guedel, M. 2002, Bulletin of the American Astronomical Society, 34, 726
 Hodgkin, S. T., & Pye, J. P. 1994, MNRAS, 267, 840
 Holman, M. J., Winn, J. N., Stanek, K. Z., et al. 2005, astro-ph/0506569
 Kuchner, M. J. 2003, ApJ, 596, L105
 Kurucz, R. 1993, ATLAS9 Stellar Atmosphere Programs and 2 km/s grid, CD-ROM No. 13
 Lakatos, S. L., Voyer, E. N., Guinan, E. F., et al. 2005, American Astronomical Society Meeting Abstracts, 206, #09.03
 Laughlin, G., Wolf, A., Vanmunster, T., et al. 2005, ApJ, 621, 1072
 Lecavelier des Etangs, A., & Vidal-Madjar, A. 2006, in *Planet Formation: Theory, Observation and Experiments*, H. Klahr & W. Brandner (Eds), Chap. 9, 147
 Lecavelier des Etangs, A., Vidal-Madjar, A., Hébrard, G., McConnell, J. 2004, A&A, 418, L1
 Léger, A., Selsis, F., Sotin, C., et al. 2004, Icarus, 169, 499
 McCullough, P., Stys, J., Valenti, J., et al. 2006, ApJ, in press, astro-ph/0605414
 Mayor, M., & Queloz, D. 1995, Nature, 378, 355
 de Pater I., Lissauer J.J. 2001, in *Planetary Sciences*, Cambridge University Press.
 Queloz, D., Eggenberger, A., Mayor, M., et al. 2000, A&A, 359, L13
 Ribas, I., Guinan, E. F., Güdel, M., & Audard, M. 2005, ApJ, 622, 680
 Rivera, E. J., Lissauer, J. J., Butler, R. P., et al. 2005, ApJ, 634, 625
 Saffe, C., Gómez, M., & Chavero, C. 2005, A&A, 443, 609
 Santos, N. C., Bouchy, F., Mayor, M., et al. 2004, A&A, 426, L19
 Santos, N. C., Pont, F., Melo, C., et al. 2006, A&A, in press (astro-ph/0601024)
 Sato, B., Fischer, D. A., Henry, G. W., et al. 2005, ApJ, 633, 465
 Schneider, J. 2006, <http://www.obspm.fr/planets>
 Tian, F., Toon, O. B., Pavlov, A. A., & De Sterck, H. 2005, ApJ, 621, 1049
 Valenti, J. 2005, HST Proposal, #10718
 Vardavas, I. M. 2005, MNRAS, 363, L51
 Vidal-Madjar, A., & Lecavelier des Etangs, A. 2004, ASP Conf. Ser. 321: Extrasolar Planets: Today and Tomorrow, 321, 152

- Vidal-Madjar, A., Lecavelier des Etangs, A., Désert, J.-M., et al. 2003, *Nature*, 422, 143
- Vidal-Madjar, A., Désert, J.-M., Lecavelier des Etangs, A., et al. 2004, *ApJ*, 604, L69
- Yelle, R. V. 2004, *Icarus*, 170, 167
- Wood, B. E., Brown, A., Linsky, J. L., et al. 1994, *ApJS*, 93, 287